

## Article

# Manganese (II) Complex of 1,4,7-Triazacyclononane-1,4,7-Triacetic Acid (NOTA) as a Hepatobiliary MRI Contrast Agent

Md. Kamrul Islam <sup>1</sup>, Ah-Rum Baek <sup>1</sup>, Byeong-Woo Yang <sup>2</sup>, Soyeon Kim <sup>3</sup>, Dong Wook Hwang <sup>4</sup>,  
Sung-Wook Nam <sup>4</sup>, Gang-Ho Lee <sup>5</sup> and Yongmin Chang <sup>2,4,6,\*</sup>

- <sup>1</sup> Institute of Biomedical Engineering Research, Kyungpook National University, Daegu 41405, Republic of Korea  
<sup>2</sup> Department of Medical and Biological Engineering, School of Medicine, Kyungpook National University, Daegu 41944, Republic of Korea  
<sup>3</sup> Division of RI-Convergence Research, Korea Institute of Radiological and Medical Sciences, Seoul 01812, Republic of Korea  
<sup>4</sup> Department of Molecular Medicine, School of Medicine, Kyungpook National University, Daegu 41944, Republic of Korea  
<sup>5</sup> Department of Chemistry, Kyungpook National University, 80, Daehak-ro, Buk-gu, Daegu 41566, Republic of Korea  
<sup>6</sup> Department of Radiology, Kyungpook National University Hospital, Daegu 41944, Republic of Korea  
\* Correspondence: ychang@knu.ac.kr; Tel.: +82-53-420-5471

**Abstract:** Magnetic resonance imaging (MRI) is increasingly used to diagnose focal and diffuse liver disorders. Despite their enhanced efficacy, liver-targeted gadolinium-based contrast agents (GBCAs) raise safety concerns owing to the release of toxic Gd<sup>3+</sup> ions. A  $\pi$ -conjugated macrocyclic chelate, **Mn-NOTA-NP**, was designed and synthesized as a non-gadolinium alternative for liver-specific MRI. **Mn-NOTA-NP** exhibits an  $r_1$  relaxivity of 3.57 mM<sup>-1</sup> s<sup>-1</sup> in water and 9.01 mM<sup>-1</sup> s<sup>-1</sup> in saline containing human serum albumin at 3 T, which is significantly greater than the clinically utilized Mn<sup>2+</sup>-based hepatobiliary drug, Mn-DPDP (1.50 mM<sup>-1</sup> s<sup>-1</sup>), and comparable with that of GBCAs. Furthermore, the in vivo biodistribution and MRI enhancement patterns of **Mn-NOTA-NP** were similar to those of the Gd<sup>3+</sup>-based hepatobiliary agent, Gd-DTPA-EOB. Additionally, a 0.05 mmol/kg dose of **Mn-NOTA-NP** facilitated high-sensitivity tumor detection with tumor signal enhancement in a liver tumor model. Ligand-docking simulations further indicated that **Mn-NOTA-NP** differed from other hepatobiliary agents in their interactions with several transporter systems. Collectively, we demonstrated that **Mn-NOTA-NP** could be a new liver-specific MRI contrast agent.

**Keywords:** magnetic resonance imaging; manganese; contrast agent; naphthalene; liver imaging



**Citation:** Islam, M.K.; Baek, A.-R.; Yang, B.-W.; Kim, S.; Hwang, D.W.; Nam, S.-W.; Lee, G.-H.; Chang, Y. Manganese (II) Complex of 1,4,7-Triazacyclononane-1,4,7-Triacetic Acid (NOTA) as a Hepatobiliary MRI Contrast Agent. *Pharmaceuticals* **2023**, *16*, 602. <https://doi.org/10.3390/ph16040602>

Academic Editors: Sara Pinto and Rafael Aroso

Received: 6 March 2023

Revised: 4 April 2023

Accepted: 11 April 2023

Published: 17 April 2023



**Copyright:** © 2023 by the authors. Licensee MDPI, Basel, Switzerland. This article is an open access article distributed under the terms and conditions of the Creative Commons Attribution (CC BY) license (<https://creativecommons.org/licenses/by/4.0/>).

## 1. Introduction

Magnetic resonance imaging (MRI) is a non-invasive technique that generates high-resolution images of the soft tissues of living organisms and has become an increasingly popular diagnostic tool in the last few decades [1–3]. Notably, high-resolution imaging techniques have considerably facilitated the detection and treatment of small liver lesions and other hepatic disorders [4,5]. Only two gadolinium-based contrast agents (GBCAs) are currently available for clinical liver MRI: gadoxetic acid (Gd-DTPA-EOB) and gadobenic acid (Gd-BOPTA). These agents use hydrophobic ligands to accumulate in hepatocytes via organic anion-transporting polypeptides (OATPs) [6]. Despite their high  $T_1$ -weighted contrast, long-term gadolinium (Gd<sup>3+</sup>) retention in the brain and bones, as well as the development of nephrogenic systemic fibrosis (NSF) in patients with impaired kidney function, has raised serious safety concerns regarding GBCAs [7,8]. Owing to these issues and the lack of non-gadolinium contrast agents (CAs) in clinical settings, feasible alternatives are required.

Multiple approaches have been employed to address the concerns regarding GBCAs, such as using Mn-based CAs, superparamagnetic iron oxide nanoparticles, chemical exchange saturation transfer imaging, X-nuclei MRI, and hyperpolarized imaging [9]. Among them, Mn-based CAs have kinetics and a biodistribution comparable with that of GBCAs in living organisms. They do not require unique pulse sequences, additional post-processing, or special equipment. Biologically active manganese (II) ( $\text{Mn}^{2+}$ ) chelates have become the focus of MRI CA studies [10–12]. Notably, complexes of biocompatible paramagnetic  $\text{Mn}^{2+}$  ions with five unpaired electrons [ $3d^5$ ] have attracted attention owing to their physical features, including delayed longitudinal electronic relaxation, shorter metal–water proton effect distances, and labile water exchange kinetics [13,14]. Additionally, homeostasis and transport in biological systems ensure effective Mn elimination [15]. Mn was the first element employed as an MRI CA in vivo, and mangafodipir trisodium (Mn-DPDP) is the only FDA-approved Mn-based chelate for liver imaging [16,17]. However, the clinical use of Mn-DPDP has been discontinued owing to its low stability. Despite the report of several stable linear  $\text{Mn}^{2+}$ -based chelates for use as hepatobiliary MRI CAs [18–22], the lack of ligand field stabilization energy in the high-spin ( $d^5$ ) electronic state has reduced the stability of the  $\text{Mn}^{2+}$  chelates [11]. Nevertheless, the increased stability of macrocyclic compounds, on the other hand, is determined by the macrocyclic effect. Therefore, macrocyclic chelates remain the most appealing option for developing highly inert Mn-based chelates.

In this study, we describe the synthesis, characterization, and in vivo biological evaluation of an amphiphilic macrocyclic  $\text{Mn}^{2+}$  chelate (**Mn-NOTA-NP**) as a biocompatible liver-specific MRI CA. The stability of **Mn-NOTA-NP** was compared with that of a linear  $\text{Mn}^{2+}$  chelate (Mn-EDTA). In addition, the lipophilic naphthalene (NP) moiety attached to the NOTA backbone by  $\pi$ -conjugation promotes hepatocyte targeting of the **Mn-NOTA-NP** chelate [23]. Hence, we demonstrated that this novel macrocyclic  $\text{Mn}^{2+}$  chelate (**Mn-NOTA-NP**) could be a feasible alternative to GBCAs for liver imaging.

## 2. Results and Discussion

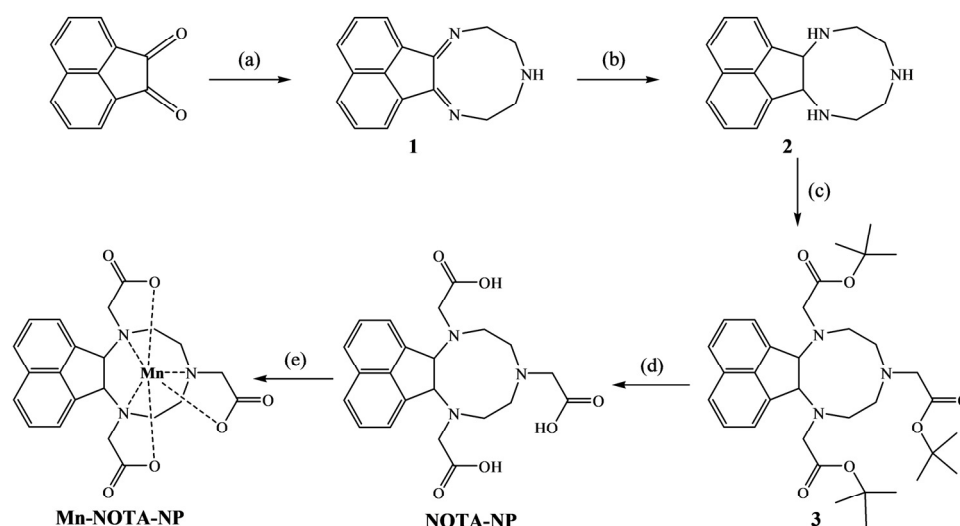
### 2.1. Synthesis and Characterization

The **NOTA-NP** ligand was synthesized by multiple-step reactions, starting with acenaphthylene-1,2-dione, and the synthetic pathway for **Mn-NOTA-NP** is depicted in Scheme 1. First, compound **2** was synthesized according to a published procedure with slight modifications [24], and alkylation with three equivalents of *tert*-butyl-bromoacetate provided protected ligand **3**. Subsequently, the *tert*-butyl group was removed using trifluoroacetic acid (TFA), and a pure chelating ligand (**NOTA-NP**) was isolated by precipitation with ether. The  $\text{Mn}^{2+}$  complex was then synthesized by reacting the ligand with an equivalent of  $\text{MnCl}_2 \cdot 4\text{H}_2\text{O}$  at pH 7.0, followed by the removal of inorganic impurities by reverse-phase chromatography. Finally, the pure chelate was collected as an off-white solid via lyophilization. The results of microanalysis and spectroscopic techniques, such as  $^1\text{H}$  NMR,  $^{13}\text{C}$  NMR, HR-FAB-MS, HR-ESI-MS, and elemental analysis, confirmed ligand and complex formation (Figures S1–S9). The purity of **Mn-NOTA-NP** was 96.05% (Figure S10).

### 2.2. Relaxivities and Human Serum Albumin (HSA)-Binding of **Mn-NOTA-NP**

The efficiency of the MRI CAs was measured in terms of their  $r_1$  and  $r_2$  relaxivities (in  $\text{mM}^{-1} \text{s}^{-1}$ ), which are defined as variations in the relaxation rate of the water protons. At 3 T, we determined the relaxivities of **Mn-NOTA-NP** and compared them with those of Mn-EDTA, Mn-DPDP, Gd-DTPA, Gd-DTPA-EOB, and Gd-BOPTA. **Mn-NOTA-NP** has an  $r_1$  value of  $3.57 \text{ mM}^{-1} \text{ s}^{-1}$ , which is 2.0-, 2.3-, and 2.4-fold higher than those of Mn-NOTA, Mn-EDTA, and Mn-DPDP, respectively (Table 1) [25,26]. NOTA, a hexadentate ligand, has three oxygen and three nitrogen donor atoms [27]. Mn-NOTA chelate is not saturated because  $\text{Mn}^{2+}$  can form seven coordinated complexes. To complete seven coordinations, a water molecule can bind in the inner sphere of the Mn chelate. In the presence of 0.67 mM HSA, the  $r_1$  relaxivity was increased to  $9.01 \text{ mM}^{-1} \text{ s}^{-1}$ , which is higher than that of Mn-EDTA and Gd-BOPTA, but relatively lower than Gd-DTPA-EOB. This suggests that it could

be used in  $T_1$ -weighted acquisitions with non-GBCAs (Table 1). The  $\pi$ -conjugated lipophilic naphthalene group facilitates albumin binding to **Mn-NOTA-NP** and slows the tumbling rate following macromolecular complex formation. Although  $\text{Mn}^{2+}$  ( $S = 5/2$ ) has fewer unpaired electrons than  $\text{Gd}^{3+}$  ( $S = 7/2$ ), the closer proximity of  $\text{Mn}^{2+}$  to the water molecules may compensate for this reduced number [28]. The  $r_2/r_1$  ratio is vital for determining the type of MRI CAs. A CA with a low  $r_2/r_1$  ratio ( $<5$ ) has a  $T_1$ -dominated contrast, whereas a CA with a high  $r_2/r_1$  ratio ( $>8$ ) has a  $T_2$ -dominated contrast [29,30].



**Scheme 1.** Synthesis of the **Mn-NOTA-NP** complex <sup>a</sup>. <sup>a</sup> Reagents and conditions: (a) Diethylenetriamine, citric acid, EtOH, 3 h, room temperature (rt); (b)  $\text{NaBH}_4$ , MeOH,  $0^\circ\text{C}$ , overnight; (c) *tert*-butyl bromoacetate,  $\text{K}_2\text{CO}_3$ , acetonitrile, rt; (d) TFA,  $\text{CH}_2\text{Cl}_2$ , 18 h, rt; (e)  $\text{MnCl}_2 \cdot 4\text{H}_2\text{O}$ , 1 M NaOH, pH = 7.0.

We also measured the binding constant ( $K_a$ ), which reflects the interaction of **Mn-NOTA-NP** with HSA (Figure S11). The binding constant  $K_a$  ( $36.6 \text{ M}^{-1}$ ) for **Mn-NOTA-NP** was comparable to the clinically used liver imaging agent **Gd-DTPA-EOB** ( $27 \text{ M}^{-1}$ ) [31]. Poor albumin binding increased relaxivity; however, it did not affect plasma enhancement.

**Table 1.** Relaxivities and lipophilicity of **Mn-NOTA-NP**, **Mn-EDTA**, **Mn-DPDP**, **Gd-DTPA**, **Gd-DTPA-EOB**, and **Gd-BOPTA** in water and human serum albumin (HSA) at 3 T (297 K).

Compound	Water			HSA (0.67 mM)			HSA Binding Constant ( $K_a$ )	logP oct/wat
	$r_1$ ( $\text{mM}^{-1} \text{ s}^{-1}$ )	$r_2$ ( $\text{mM}^{-1} \text{ s}^{-1}$ )	$r_2/r_1$	$r_1$ ( $\text{mM}^{-1} \text{ s}^{-1}$ )	$r_2$ ( $\text{mM}^{-1} \text{ s}^{-1}$ )	$r_2/r_1$		
<b>Mn-NOTA-NP</b>	$3.57 \pm 0.20$	$18.08 \pm 0.50$	5.0	$9.01 \pm 0.50$	$42.83 \pm 2.70$	4.8	$36.6 \text{ M}^{-1}$	−0.93
<b>Mn-EDTA</b>	$1.79 \pm 0.05$	$3.85 \pm 0.05$	2.2	$2.93 \pm 0.30$	$5.54 \pm 0.10$	1.9	-	−2.72
<b>Mn-DPDP</b> <sup>b</sup>	$1.50 \pm 0.40$	$2.30 \pm 0.60$	1.5	-	-	-	-	−3.07
<b>Gd-DTPA</b>	$4.12 \pm 0.10$	$5.20 \pm 0.20$	1.3	-	-	-	-	−3.16
<b>Gd-DTPA-EOB</b> <sup>b</sup>	$4.30 \pm 0.60$	$5.50 \pm 0.60$	1.3	$9.97 \pm 1.00$	$10.76 \pm 0.10$	1.1	$27 \text{ M}^{-1}$	−2.11
<b>Gd-BOPTA</b> <sup>b</sup>	$4.00 \pm 0.60$	$4.70 \pm 0.60$	1.2	$8.27 \pm 0.10$	$10.84 \pm 0.10$	1.3	-	−2.23

<sup>b</sup> Data were obtained from the cited reference [32].

### 2.3. Lipophilicity of **Mn-NOTA-NP**

Most  $\text{Gd}^{3+}$  complexes are confined to extracellular spaces and cannot enter cells owing to their high hydrophilicity. Typically, the biological activity of compounds increases as their lipophilicity increases owing to their attraction to biological membranes and increased permeability, allowing for greater access to the desired location inside the body [33]. We hypothesized that conjugating a lipophilic moiety to a cell-impermeable metal complex would yield an amphiphilic combination that could pass through cell membranes. The

clinically applied liver imaging agent, Gd-DTPA-EOB, also comprises a hydrophilic Gd-DTPA derivative coupled with a lipophilic ethoxybenzyl (EOB) moiety. Gale et al. reported that the log P values of a series of small-molecule Mn (II) complexes are closely correlated with the blood clearance rate and liver accumulation [22]. The lipophilicity of **Mn-NOTA-NP** was estimated using octanol-water partitioning coefficient (log P) measurements. **Mn-NOTA-NP** has log *p* values of  $-0.93$ , which are 61 and 138 times greater than those of Mn-EDTA ( $-2.72$ ) and Mn-DPDP ( $-3.17$ ), respectively (Table 1). Furthermore, the log P value of **Mn-NOTA-NP** was 15–20 times higher than the log P values of the clinically used Gd-based agents, Gd-DTPA-EOB ( $-2.11$ ) and Gd-BOPTA ( $-2.23$ ) (Table 1).

#### 2.4. Kinetic Inertness and pH Stability of **Mn-NOTA-NP**

The kinetic inertness of metal complexes is more crucial than their thermodynamic stability for in vivo applications [14,34]. Thus, the transmetalation process between **Mn-NOTA-NP** and  $Zn^{2+}$  ions was examined using a previously published method [35]. As zinc ( $Zn^{2+}$ ) is the second most abundant trace metal in the human body, it can disrupt more  $Mn^{2+}$  ions than trace metals, such as  $Cu^{2+}$  and  $Ca^{2+}$ . Furthermore, as the transmetalation process occurs more frequently, the chelation between the ligand and metal becomes increasingly unstable. In the current study, the kinetic inertness of **Mn-NOTA-NP** was represented by the transverse relaxivity change [ $\Delta r_2(t) = r_2(t) - r_2(0)$ ] as a function of time. For comparison, Mn-EDTA, Gd-DTPA, and Gd-DTPA-EOB were also assessed (Figure 1). To demonstrate this, the complexes were subjected to a tenfold excess of  $Zn^{2+}$ , and the  $\Delta r_2(t)$  values of the  $Mn^{2+}$  and  $Gd^{3+}$  complexes were compared. As shown in Figure 1, the  $\Delta r_2(t)$  values of Mn-EDTA and Gd-DTPA rapidly increased and saturated at high  $\Delta r_2$  values. In contrast, **Mn-NOTA-NP** began with a quickly increasing  $\Delta r_2(t)$  value, but shortly reached saturation at significantly lower  $\Delta r_2$  values and maintained its relaxation rate, implying that transmetalation occurred much less frequently after that point. These data indicate that **Mn-NOTA-NP** is more resistant to  $Zn^{2+}$  transmetalation than Mn-EDTA and Gd-DTPA, as evidenced by its rapid dissociation. An earlier manganese-based liver imaging agent, mangafodipir (Mn-DPDP), was licensed for liver imaging, but this form of chelated Mn acted as a prodrug and released free  $Mn^{2+}$  upon administration [36]. Moreover, the  $\Delta r_2(t)$  pattern of Gd-DTPA-EOB increased over time and reached saturation at relatively low  $r_2$  values, although after 4 h, the  $\Delta r_2(t)$  pattern of **Mn-NOTA-NP** was comparable to that of Gd-DTPA-EOB. This result suggests that **Mn-NOTA-NP** is more susceptible to  $Zn^{2+}$  transmetalation than Gd-DTPA-EOB.

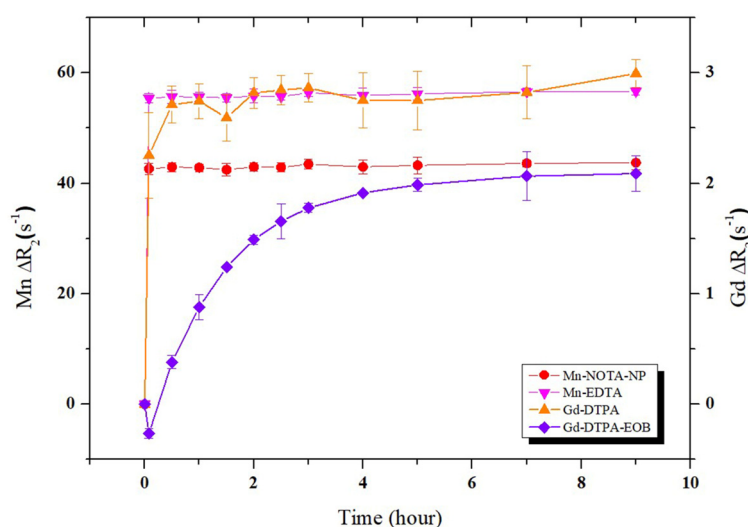


**Figure 1.** Transmetalation kinetics of 1 mM **Mn-NOTA-NP** (●), Mn-EDTA (▼), Gd-DTPA (▲), and Gd-DTPA-EOB (■) over 10 mM  $Zn^{2+}$  plotted by  $\Delta R_2$  as a function of time at 3 T and 293 K. Data are presented as  $n = 4$  and mean  $\pm$  SD (standard deviation).

Furthermore, the stability of **Mn-NOTA-NP** was assessed over time by measuring the  $r_2$  relaxivity in phosphate-buffered solutions (PBS) with pH values ranging from 1.0 to 10.0 (Figure S12). The  $r_2$  values remained steady over a wide pH range (up to 10.0); however, at pH 7, the  $r_2$  relaxivity decreased significantly compared to its initial values. These observations are to be anticipated when evoking the potential displacement of the inner-sphere water molecule by the phosphate anion of PBS [37]. Altering the complex pH from basic to acidic, i.e., from pH 4 to lower, increased the  $r_2$  values. Complex dissociation may be attributed to the increased relaxivity at a low pH, which is in line with an earlier study [25]. Thus, we believe that **Mn-NOTA-NP** is suitable for in vivo investigations and may be an appropriate substitute for GBCAs, particularly in populations with a compromised renal function where gadolinium exposure is a concern.

### 2.5. Protein–Ligand Docking Simulations of **Mn-NOTA-NP**

The molecular docking approach replicates the atomic interaction between a small molecule and a protein, allowing us to quantitatively investigate small-molecule behavior at target protein binding sites and elucidate critical biological processes [38]. Gd-DTPA-EOB is taken up by hepatocytes through OATPs (mostly OATP1B1 and OATP1B3) and discharged into bile canaliculi through multidrug resistance-associated protein 2 (MRP2) [39]. The activity of these transporters influences the metabolic and biliary clearance of drugs. Consequently, they can affect pharmacological efficacy or toxicity by affecting plasma concentration [40]. We postulated that OATPs could mediate the hepatic uptake of **Mn-NOTA-NP** because of their similar biodistribution pattern to Gd-DTPA-EOB [41]. The expression and localization of OATP1B1 and/or -1B3 and MRP2 in tumors may influence the degree of hepatocyte-selective enhancement. Therefore, AutoDock Vina was used to predict the protein–ligand docking simulations.

The interactions between various transporter systems and **Mn-NOTA-NP** are displayed in Figure 2. **Mn-NOTA-NP** establishes a network of hydrogen bonds with the residues surrounding the OATP1B1 transporter, including N446, K49, and T338 (yellow dotted line) (Figure 2a). In addition, **Mn-NOTA-NP** interacts with OATP1B3 via hydrogen bonds at N446 and K49 (Figure 2b). For comparison, computational docking investigations of the commercially available hepatobiliary drug Gd-DTPA-EOB, as well as the previously reported Mn-EDTA-BTA and Mn-EDTA-EOB, are shown in Figures S13 and S14 [19]. Mn-EDTA-BTA forms hydrogen bonds with N446 and K49 to bind to the OATP1B1 transporter, and with N446, K49, N335, R290, S450, and K497 to bind to OATP1B3. Mn-EDTA-EOB forms multiple hydrogen bonds with the OATP1B3 transporter, and K49 forms a salt bridge with the metal complex. Gd-DTPA-EOB comprises several hydrogen bonds and salt bridges that bind to OATP1B1 and OATP1B3. **Mn-NOTA-NP** binds to a U-shaped motif composed of amino acids 1435–1442 in the MRP2 transporter (Figure 2c). Mn-EDTA-BTA, Mn-EDTA-EOB, and Gd-DTPA-EOB use the U-shaped motif of amino acids 1435–1442 as the binding site and form a hydrogen bond between R1442 and the metal complex (yellow dotted line) (Figures S13 and S14).

The AutoDock Vina scoring function was used to calculate the binding free energies of these compounds (Table 2). The docking scores of **Mn-NOTA-NP** with OATP1B1 and OATP1B3 were 9.281 and 5.532 kcal/mol, respectively. Furthermore, the docking score between **Mn-NOTA-NP** and the MRP2 transporter was 4.579 kcal/mol, which was higher than that of Gd-DTPA-EOB (3.976 kcal/mol), but lower than that of Mn-EDTA-BTA (5.731 kcal/mol) and Mn-EDTA-EOB (5.149 kcal/mol). Therefore, based on the docking analysis, the best transporter system for Mn-EDTA-BTA and Mn-EDTA-EOB was OATP1B3, whereas those of Gd-DTPA-EOB were OATP1B1 and OATP1B3. The docking simulation results revealed that **Mn-NOTA-NP** differed from the other investigated compounds in its interaction with the transporters. According to this finding, OATP1B1 is a crucial transporter for **Mn-NOTA-NP** absorption. Although OATP1B1 and OATP1B3 are expressed in normal liver tissues, their expression is reduced in primary and metastatic liver cancers [42].

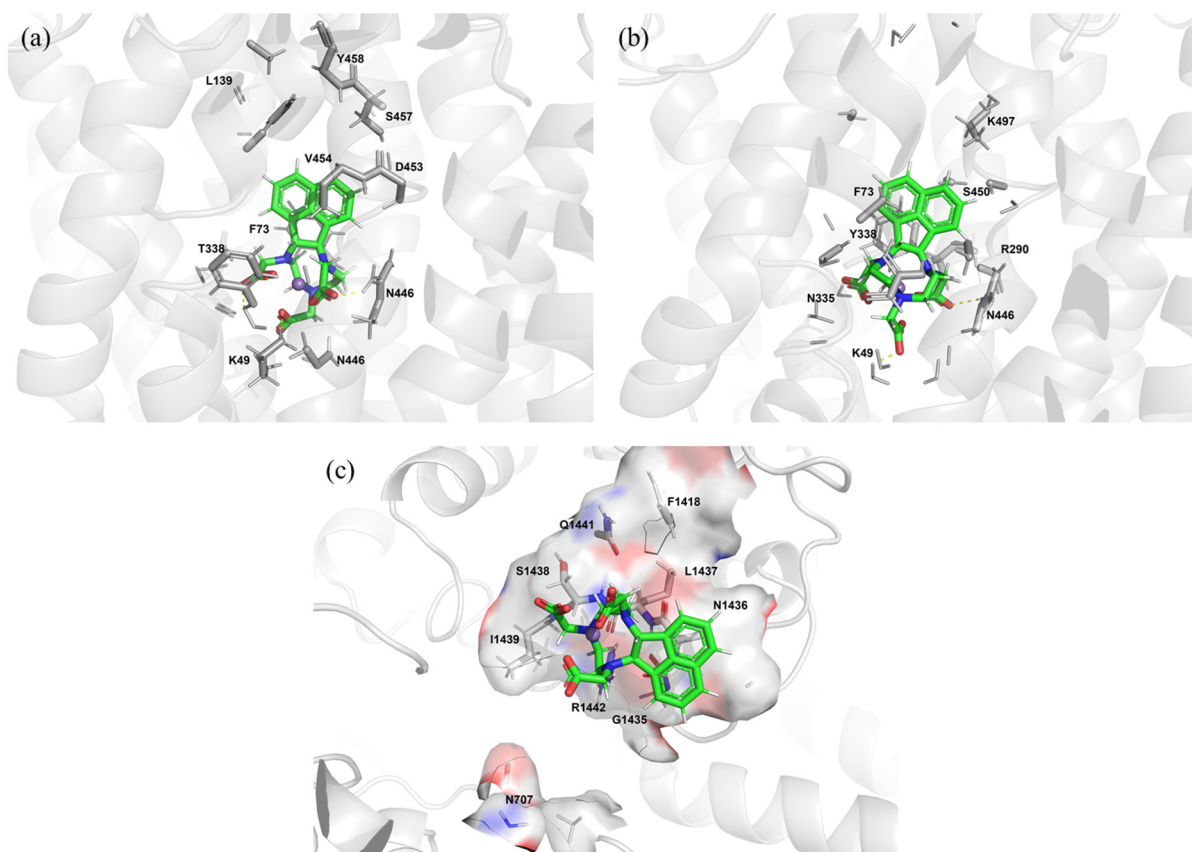


**Figure 2.** Schematic representations of variable interactions between **Mn-NOTA-NP** and (a) OATP1B1, (b) OATP1B3, and (c) MRP2. The yellow line represents hydrogen bonds.

**Table 2.** Docking scores for **Mn-NOTA-NP**, **Mn-EDTA-BTA**, **Mn-EDTA-EOB**, and **Gd-DTPA-EOB** with organic anion-transporting polypeptides (OATPs) and multidrug resistance-associated protein 2 (MRP2). Data expressed as kcal/mol.

Compounds	OATP1B1	OATP1B3	MRP2
<b>Mn-NOTA-NP</b>	−9.281	−5.532	−4.579
Gd-DTPA-EOB <sup>c</sup>	−13.25	−11.54	−3.976
Mn-EDTA-BTA	−7.392	−10.172	−5.731
Mn-EDTA-EOB <sup>c</sup>	−9.36	−11.58	−5.149

<sup>c</sup> Data collected from the cited reference [19].

## 2.6. Cytotoxicity of **Mn-NOTA-NP**

CCK-8 assays were used to assess the cytotoxic effects of **Mn-NOTA-NP** on the RAW 264.7 cell line. Cells were cultured for 24 h at 37 °C, with various doses of **Mn-NOTA-NP** and **Gd-DTPA** as controls (Figure 3). CCK-8 assays revealed that the cells were viable at increasing **Mn-NOTA-NP** concentrations up to 50  $\mu$ M and 200  $\mu$ M, which remained above 86% and 82%, respectively. Although **Mn-NOTA-NP** showed a decrease in cell viability at high concentrations, these findings indicate that **Mn-NOTA-NP** has negligible cytotoxicity at the amounts required for an optimal MRI signal.

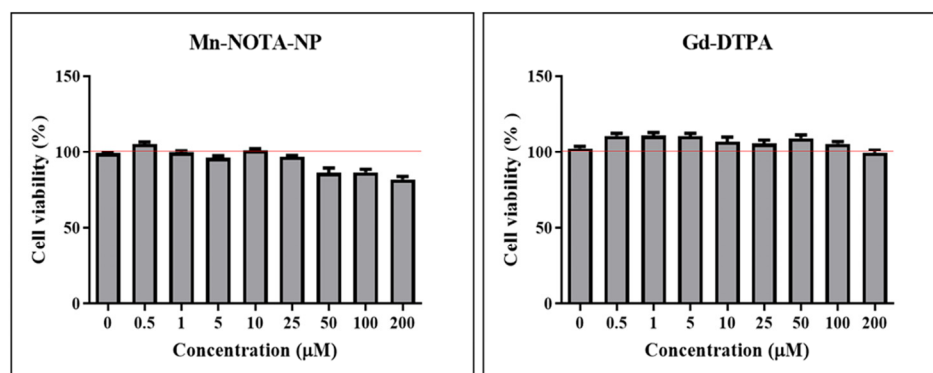


**Figure 3.** In vitro cell viability of RAW 264.7 cells with different concentrations of **Mn-NOTA-NP** and Gd-DTPA at 37 °C for 24 h. Data are represented as mean  $\pm$  SEM (standard error of the mean) and  $n = 3$ . The red line represents the control value.

### 2.7. In Vivo MR Images of Normal Mice Using **Mn-NOTA-NP**

To test the hepatobiliary imaging capability of **Mn-NOTA-NP**, we performed in vivo MRI experiments in Balb/c mice after intravenous injection of **Mn-NOTA-NP** at 3.0 T and Gd-DTPA-EOB as a reference agent.  $T_1$ -weighted coronal images of the liver (Figure 4A) and kidneys (Figure 4B) were taken before injection and at 5, 10, 20, and 30 min and 1 and 2 h after injection. Additionally, the signal strengths in the liver and kidneys were monitored, and the signal-to-noise ratio (SNR) was measured as a function of time to analyze the contrast enhancement patterns in vivo (Figure 4C,D). The most characteristic MR feature demonstrates significant and prolonged contrast enhancement in the liver after injection of (a) **Mn-NOTA-NP** or (b) Gd-DTPA-EOB at 0.05 and 0.025 mmol/kg, respectively. In vivo, MRI revealed that **Mn-NOTA-NP** has a dual pathway for excretion, which is highly similar to the clinically used Gd-DTPA-EOB. Moreover, the SNRs of **Mn-NOTA-NP** and Gd-DTPA-EOB in the liver were comparable up to 2 h after injection (Figure 4C). Notably, the injection dose of Gd-DTPA-EOB was lower than that of **Mn-NOTA-NP** in the current study because the injection dose of Gd-DTPA-EOB could not be increased owing to the risk of NSF [7,43].

Additionally, **Mn-NOTA-NP** and Gd-DTPA-EOB exhibited similar kidney signals for up to 30 min, indicating their renal excretion (Figure 4B). As demonstrated by an increase in the kidney signal after 30 min, the renal excretion of **Mn-NOTA-NP** was slightly higher than that of Gd-DTPA-EOB (Figure 4D). Overall, **Mn-NOTA-NP** with an amphiphilic negatively charged structure displayed optimal liver-specific contrast enhancement and a combination of hepatobiliary and renal clearance in this in vivo imaging study.

### 2.8. In Vivo Biodistribution of **Mn-NOTA-NP**

An in vivo biodistribution study was conducted to measure the concentration of  $Mn^{2+}$  ions in the brain, heart, gallbladder, liver, kidneys, spleen, and intestine using Inductively Coupled Plasma Emission Spectrometry (ICP-OES) (Figure 5). The  $Mn^{2+}$  levels were highest in the liver (approximately 54%) and intestine at 15 min, indicating that **Mn-NOTA-NP** was removed via the hepatobiliary pathway. **Mn-NOTA-NP** demonstrated a similar liver accumulation at 30 min compared to the clinically used liver-targeting agent Gd-DTPA-EOB [44,45]. Subsequently, it was rapidly removed from the liver. In addition to the liver, the kidneys also showed a high Mn accumulation owing to glomerular excretion via the renal pathway. Consequently, the in vivo biodistribution findings strongly imply that **Mn-NOTA-NP** is excreted via the hepatobiliary and renal pathways, similar to the liver-specific agent Gd-DTPA-EOB. Notably, the Mn levels were almost restored to the control levels 24 h after the **Mn-NOTA-NP** injection.

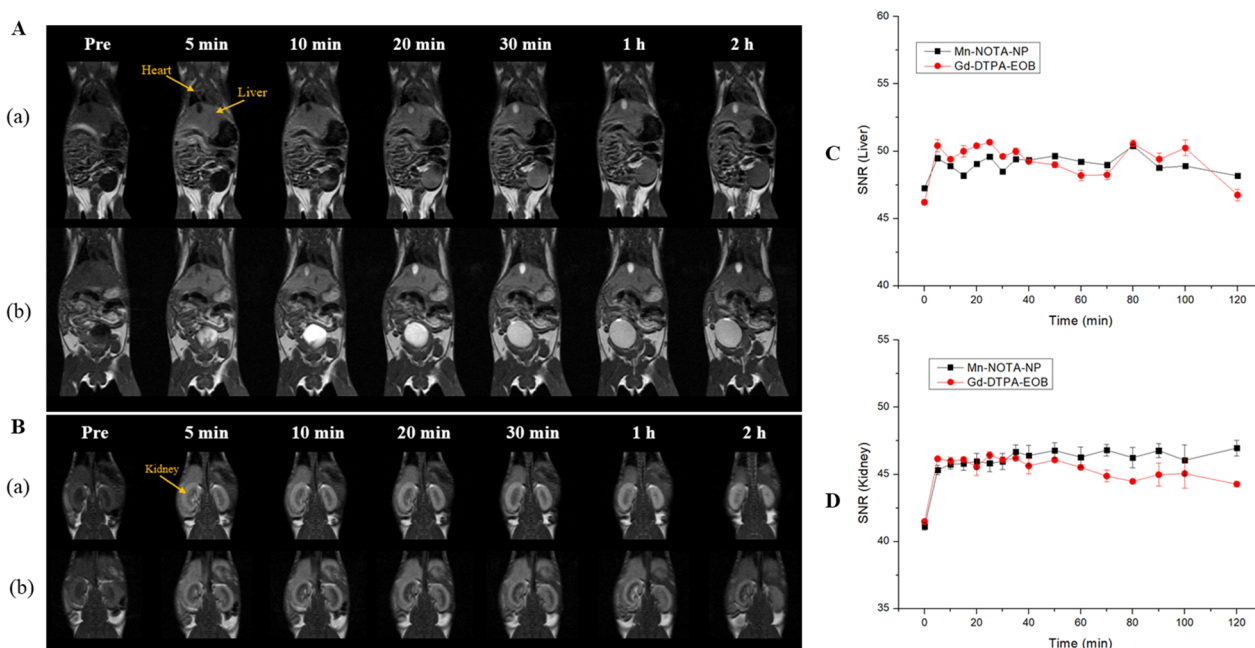


**Figure 4.**  $T_1$ -weighted images of Balb/c mice recorded at 3.0 T capturing the (A) liver and (B) kidneys obtained before injection (pre) and at 5, 10, 20, and 30 min and 1 and 2 h after tail vein injection of (a) Mn-NOTA-NP and (b) Gd-DTPA-EOB at a dose of 0.05 and 0.025 mmol/kg, respectively. The graphs depict the signal-to-noise ratio (SNR) profiles of Mn-NOTA-NP (black squares) and Gd-DTPA-EOB (red circles) in the (C) liver and (D) kidneys after injection. Data are presented as mean  $\pm$  SD and  $n = 3$ .

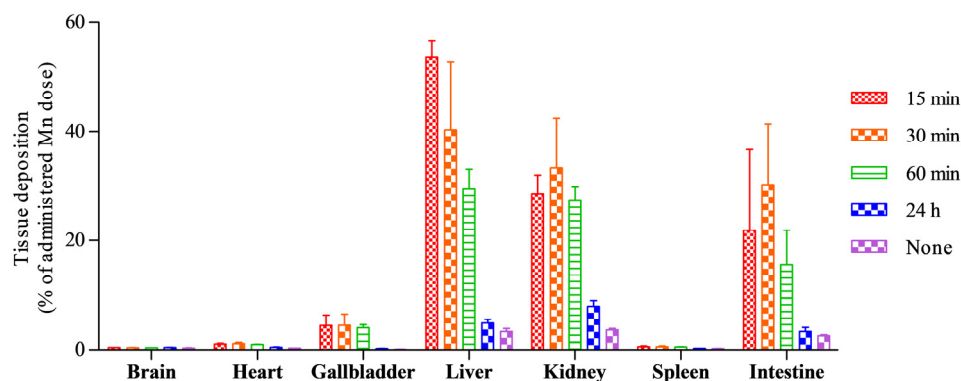


**Figure 5.** In vivo biodistribution patterns of Mn-NOTA-NP (0.05 mmol Mn/kg) in Balb/c mice, expressed as the percentage of Mn concentrations in each tissue ( $n = 4$ ). Mice were sacrificed at 15 min, 30 min, 60 min, and 24 h. Untreated mice served as controls and were labeled as “None.” Data are presented as mean  $\pm$  SD.

### 2.9. In Vivo MR Images of the Liver Tumor Model Using Mn-NOTA-NP

To assess the possible clinical application of the Mn-NOTA-NP chelate as a liver-specific CA, we performed in vivo MRI following tail vein injection using a HepG2 orthotopic mouse model of human hepatocellular carcinoma (HCC). Before administering Mn-NOTA-NP,  $T_1$ -weighted MR images of the liver parenchyma and HCC tissues displayed indistinguishable and nonspecific iso-signal intensities. MR images captured 5 min after Mn-NOTA-NP injection revealed that tumor tissues could be distinguished from normal liver parenchyma because tumor tissues have a higher signal strength than normal liver parenchyma (Figure 6a). Furthermore, the HCC tissue appeared significantly hyperintense in the liver parenchyma tissue on the  $T_1$ -weighted images, with high tumor signal intensity 2 h after injection of the Mn-NOTA-NP chelate. As a result, Mn-NOTA-NP-enhanced MRI

would result in an elevated tumor-to-normal liver contrast ratio with high tumor detection sensitivity, allowing for the early diagnosis of HCC (Figure 6b).

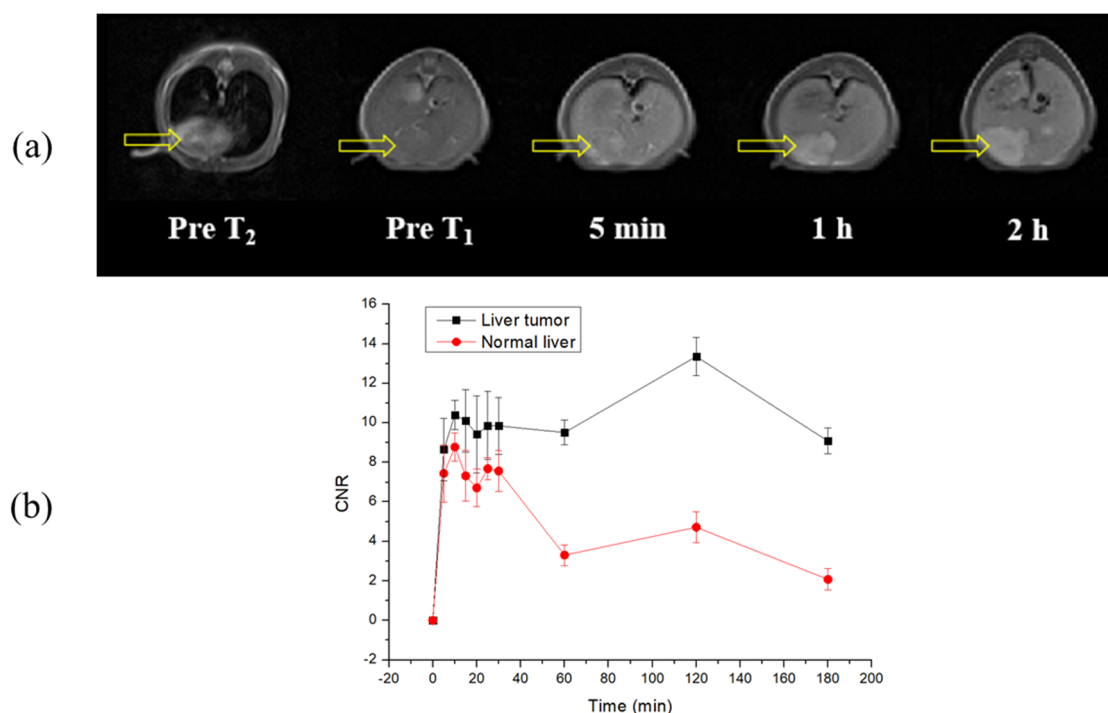


**Figure 6.** Axial T<sub>2</sub>- and T<sub>1</sub>-weighted MR images of HepG2 orthotopic mice (a) before injection and 5 min, 1 h, and 2 h post injection of Mn-NOTA-NP (0.05 mmol/kg); yellow arrows show the liver tumor lesions. (b) Difference of contrast-to-noise ratio (CNR) between liver tumor tissue (black squares) and normal liver parenchyma (red circles) as a function of time.

Based on the molecular docking results, one possible explanation for the high tumor-to-normal liver contrast ratio after using Mn-NOTA-NP is the different roles of OATPs and MRP2 expression in HCC. First, Mn-NOTA-NP-enhanced MR images exhibited signal enhancements in both normal liver and HCC cells, suggesting that OATP1B1/B3 mediates the uptake of Mn-NOTA-NP from the sinusoid into the normal liver (hepatocytes) and HCC cells [6,46]. Second, HCC signal enhancement was MRP2-dependent when OATP1B1/B3 expression was maintained. As MRP2 mediates the secretion of Mn-NOTA-NP from tumor cells to the lumen, the decreased MRP2 expression in tumor cells results in the accumulation of Mn-NOTA-NP in the cytoplasm of tumor cells; thus, HCCs are hyperintense compared with the normal liver [47]. According to Ni et al., this persistent tumor enhancement could be valuable in distinguishing HCC from other liver disorders and determining HCC cellular differentiation [46,48]. However, further investigation is required to clarify the detailed mechanism of tumor enhancement by Mn-NOTA-NP.

### 3. Materials and Methods

#### 3.1. Reagents and Materials

The solvents were purified and dried using standard procedures. Acenaphthoquinone, diethylenetriamine, and MnCl<sub>2</sub>·4H<sub>2</sub>O were purchased from Sigma-Aldrich (St Louis, MO, USA) and used without further purification. Unless otherwise specified, all other commercial reagents were purchased from Sigma-Aldrich or Tokyo Chemical Industry Co., Ltd. (Tokyo, Japan) and used in the original forms. Deionized water was used in all experiments. The reactions were followed by thin-layer chromatography (TLC) using silica gel plates 60 F254 (Merck, Darmstadt, Germany) and UV light for visualization. <sup>1</sup>H NMR (500 Hz) and <sup>13</sup>C NMR (126 Hz) experiments were performed using a Bruker Avance

500 spectrometer at the Center for Instrumental Analysis, Kyungpook National University (KNU), Daegu, Korea. As an internal standard, the chemical shifts were presented as  $\delta$  values of tetramethylsilane. The coupling constants are expressed in hertz. Elemental analysis was conducted at the Center for Instrumental Analysis at KNU. High-resolution fast-atom bombardment mass spectrometry (HR-FAB-MS; JMS-700, JEOL, Tokyo, Japan) and electrospray ionization time-of-flight MS (ESI-TOF-MS; SYNAPT G2, Waters, USA) were performed at the Korea Basic Science Institute. A high-pressure liquid chromatography (HPLC; LC/Forte/R, YMC, Iwata, Japan) system equipped with a Luna C18 column (250 mm  $\times$  21.2 mm, Phenomenex Inc., Torrance, CA, USA) was used for further purification. The conditions used to validate purity were as follows: eluent A, 10 mM ammonium acetate in water; eluent B, 10 mM ammonium acetate in acetonitrile; gradient, 5–40% B in 3 min, 40–80% B in 25 min, and 80–100% B in 3 min; flow rate, 12 mL/min. HPLC was performed using UV-Vis detection at 254 nm. The purity of the products was determined to be over 95% using elemental analysis and HPLC spectra. No unanticipated or exceptionally substantial safety risks were identified during the experimental procedures.

### 3.2. Synthesis and Characterization

#### 3.2.1. Synthesis of Compound 2

The title compound was prepared using a previously reported method with slight modifications [24]. Briefly, acenaphthylene-1,2-dione (1.0 g, 5.48 mmol) was combined with diethylenetriamine (0.57 g, 5.48 mmol) in a mixture of ethanol and deionized (DI) water in a 3:1 ratio. The mixture was then agitated for 3 h with a 5-mole percent citric acid solution before being filtered. The solvent was removed, and the product was washed with acetonitrile before reusing it. Subsequently, compound 1 was dissolved in methanol, and  $\text{NaBH}_4$  was added in portions at 0 °C. The solvent was removed, and  $\text{CH}_2\text{Cl}_2$  was used for extraction. The organic layer was dried over  $\text{NaSO}_4$  and then vacuumed. Using DCM:MeOH as the eluent, flash chromatography was performed to obtain a pale-yellow solid product with a yield of 78%.  $^1\text{H}$  NMR (500 MHz,  $\text{DMSO-d}_6$ ):  $\delta$  (ppm) = 8.43–8.41 (*d*, 2H, CH, naphthalene), 8.29–8.28 (*d*, 2H, CH, naphthalene), 7.80–7.77 (*t*, 2H, CH, naphthalene), 4.35 (*s*, 2H, CH-NH), 4.12 (*t*, 2H,  $-\text{CH}_2$ ), 3.44 (*t*, 4H,  $-\text{CH}_2$ ), 2.89 (*t*, 2H,  $-\text{CH}_2$ ).  $^{13}\text{C}$  NMR (126 MHz,  $\text{CDCl}_3$ ):  $\delta$  = 127.94, 125.53, 122.24, 119.40, 67.99, 30.33, 25.62. HR-FAB-MS calculated for  $\text{C}_{16}\text{H}_{19}\text{N}_3$ : 254.1657  $[\text{M} + \text{H}]^+$ ; observed: 254.1657  $[\text{M} + \text{H}]^+$ .

#### 3.2.2. Synthesis of Compound 3

Compound 2 (1.0 g, 3.94 mmol) was dissolved in acetonitrile, and  $\text{K}_2\text{CO}_3$  (3.26 g, 23.62 mmol) was added to the solution. Subsequently, *tert*-butyl bromoacetate (2.30 g, 11.81 mmol) was added dropwise for 30 min, and the mixture was stirred overnight at room temperature. The resulting mixture was filtered, and the solvent was removed to obtain a crude product. Compound 3 was purified by column chromatography (silica gel, hexane/EtOAc, 9:1) and collected as an oily solid; the yield was 1.41 g (61%).  $^1\text{H}$  NMR (500 MHz,  $\text{MeOH-d}_4$ ):  $\delta$  (ppm) = 8.46–7.40 (*m*, 6H, naphthalene), 5.39 (*s*, 2H, CH), 5.21–4.84 (*m*, 1H, CH), 4.65–3.39 (*m*, 5H, CH), 3.35–3.25 (*m*, 3H,  $\text{CH}_2$ ), 3.13–1.86 (*m*, 5H,  $\text{CH}_2$ ), 1.43–1.18 (*m*, 27H,  $\text{CH}_3$ ). CHN Anal. Calcd. for  $\text{C}_{34}\text{H}_{49}\text{N}_3\text{O}_6 \cdot \text{K}_2\text{CO}_3$ : C, 57.27; H, 6.73; N, 5.73; observed: C, 57.57; H, 6.82; N, 6.15. HR-FAB-MS calculated for  $\text{C}_{34}\text{H}_{49}\text{N}_3\text{O}_6$ : 596.3700  $[\text{M} + \text{H}]^+$ ; observed: 596.3696  $[\text{M} + \text{H}]^+$ .

#### 3.2.3. Synthesis of NOTA-NP

Deprotection of *tert*-butyl was performed as follows: compound 3 (1.0 g, 1.68 mmol) was dissolved in a mixture of trifluoroacetic acid and  $\text{CH}_2\text{Cl}_2$  at 0 °C and stirred for 18 h. The solution was evaporated under reduced pressure, and ether was added to obtain the precipitate. The product was then filtered, washed with ether several times, and vacuum-dried, and the pure product was collected as an off-white solid. The yield was 0.63 g (88%).  $^1\text{H}$  NMR (500 MHz,  $\text{MeOH-d}_4$ ):  $\delta$  (ppm) = 7.86–7.84 (*d*, 1H, CH, naphthalene), 7.78–7.76 (*d*, 2H, CH, naphthalene), 7.58–7.53 (*m*, 3H, CH, naphthalene), 5.35–5.33 (*d*, 1H, CH), 5.21–5.19

(*d*, 1H, CH), 4.01–3.51(*m*, 6H, CH<sub>2</sub>), 3.40–3.25 (*m*, 4H, CH), 3.16–3.13 (*m*, 2H, CH), 2.87–2.84 (*m*, 2H, CH). <sup>13</sup>C NMR (126 MHz, MeOH-*d*<sub>4</sub>): δ = 174.08, 172.60, 138.15, 131.51, 128.28, 127.70, 126.82, 125.00, 123.15, 122.03, 64.68, 64.20, 54.84, 54.73, 49.12, 44.61, 42.29. CHN Anal. Calcd. for C<sub>22</sub>H<sub>25</sub>N<sub>3</sub>O<sub>6</sub>·1.5 CF<sub>3</sub>COOH: C, 50.44; H, 4.50; N, 7.09; observed: C, 50.09; H, 4.43; N, 7.32. HR-FAB-MS calculated for C<sub>22</sub>H<sub>25</sub>N<sub>3</sub>O<sub>6</sub>: 428.1822 [M + H]<sup>+</sup>; observed: 428.1824 [M + H]<sup>+</sup>.

### 3.2.4. Synthesis of Mn-NOTA-NP

Ligand **NOTA-NP** (0.32 g, 0.75 mmol) was dissolved in DI water, and the pH of the solution was adjusted to 7.0 by dropwise addition of 1 M NaOH. The solution of MnCl<sub>2</sub>·4H<sub>2</sub>O (0.15 g, 0.75 mmol) was added slowly, and the resulting suspension was stirred for 24 h at room temperature. The pH of the resulting mixture was readjusted to 7.0 several times. The solid was filtered and vacuum dried to obtain a crude solid product, which was further purified using preparative HPLC, and the purity was confirmed. The yield was 0.16 g (45%). CHN Anal. Calcd. for C<sub>22</sub>H<sub>22</sub>MnN<sub>3</sub>O<sub>6</sub>·3H<sub>2</sub>O: C, 49.54; H, 5.29; N, 7.88; observed: C, 49.37; H, 5.14; N, 8.57. HR-ESI-MS calculated for C<sub>22</sub>H<sub>22</sub>MnN<sub>3</sub>O<sub>6</sub>: 479.0889 [M]<sup>+</sup>; observed: 479.0889 [M]<sup>+</sup>.

### 3.3. Relaxivity

*T*<sub>1</sub> measurements were obtained on a 3 T MRI scanner (Architect, GE Healthcare, US) using an inversion recovery method with variable inversion times (TIs). The magnetic resonance (MR) images were captured at 35 different times between 50 and 1750 ms. The signal intensity at each TI value was fitted nonlinearly to obtain the corresponding *T*<sub>1</sub> relaxation time. For the *T*<sub>2</sub> measurements, the Carr–Purcell–Meiboom–Gill (CPMG) pulse sequence was adapted for multiple spin-echo sizes. In total, 34 different echo time (TE) values ranging from 10 to 1900 ms were used to capture the corresponding images. First, the *T*<sub>2</sub> relaxation times were derived from a nonlinear least-squares fit of the average pixel values for multiple spin-echo measurements at each TE. Subsequently, the relaxation times (*T*<sub>1</sub> and *T*<sub>2</sub>) were image-processed to generate a relaxation time map. Finally, the relaxivities (*r*<sub>1</sub> and *r*<sub>2</sub>) were measured as the inverse of the relaxation time per mM.

### 3.4. Octanol–Water Partition Coefficients

We adopted a previously described method to measure the octanol–water partition coefficients [19]. Briefly, 1 mg of **Mn-NOTA-NP** was dissolved in 2 mL of water and 1-octanol (1:1 mixture). The vial containing the mixture was shaken for 30 s and placed on a rotator for gentle mixing to equilibrate for 48 h. After mixing, the sample was allowed to settle at room temperature for 24 h. Each layer of the Mn<sup>2+</sup> concentration was determined using inductively coupled plasma-mass spectrometry (ICP-MS). The partition coefficients were calculated from the equation  $\log P = \log (C_o/C_w)$ , where  $\log P$  is the logarithm of the partition coefficient, and *C*<sub>o</sub> and *C*<sub>w</sub> are the concentrations of Mn in the 1-octanol and water layers, respectively.

### 3.5. Determination of Binding Constants

The binding affinity of the **Mn-NOTA-NP** chelate to human serum albumin (HSA) was determined using a previously published protocol [20]. A nonlinear increase in the proton paramagnetic relaxation rates for solutions containing 0.67 mM HSA at 64 MHz was fitted using the following equation:

$$R_1^{p^{obs}} = 1000 \times \left\{ \left( r_1^f s^0 \right) + \frac{1}{2} \left( r_1^c - r_1^f \right) \left( (Np^0) + s^0 + K_a^{-1} - \sqrt{\left( (Np^0) + s^0 + K_a^{-1} \right)^2 - 4N \times s^0 \times p^0} \right) \right\}$$

where  $N$  is the number of independent interaction sites ( $N = 1$ ),  $K_a$  is the HSA binding constant,  $p^0$  is the HSA concentration,  $s^0$  is the complex paramagnetic concentration, and  $r_1^c$  and  $r_1^f$  are the relaxivities of the complex containing HSA and a free agent, respectively.

### 3.6. Transmetalation Kinetics

This experiment was performed using a previously reported method with slight modifications [35]. A total of 20 microliters of a 50 mM MES [2-(N-morpholino)ethanesulfonic acid] buffered solution (pH 6.0) of  $ZnCl_2$  was added to 1 mL of a buffered solution of the 1 mM Mn complex. The mixture was shaken for a while and immediately used to measure the solvent  $T_2$  as a function of time. Control studies were also conducted with Mn-EDTA, Gd-DTPA (Magnevist®), and Gd-DTPA-EOB (Primovist®) for comparison. The measurements were performed on a 3 T MRI scanner (Discovery MR750w 3.0 T, GE Healthcare, Chicago, IL, USA) at room temperature.

### 3.7. pH Stability

The pH-dependent changes in the longitudinal relaxation rate of **Mn-NOTA-NP** were evaluated on a scale ranging from pH 1 to 10. Samples of each pH buffer solution (pH 1, 4, 7, and 10) were brought from Daejung Chemicals (Siheung-si, Korea). The experiment was performed at room temperature for 72 h on a 3T system (128 MHz, Magnetom Tim Trio, Siemens, Korea Institute of Radiological and Medical Science). First, 950  $\mu$ L of the buffer solution and 50  $\mu$ L of the compound were added to a final volume of 1 mL. The pH was then adjusted using negligible volumes of diluted HCl/NaOH to decrease or increase the pH of the acidic and basic ranges while maintaining a constant complex concentration throughout the experiments. The imaging parameters for spin-echo images were as follows: TR = 2000; TE = 15; voxel size =  $0.75 \times 0.75 \times 5.0$  mm; 5.0 slice thickness; FOV read = 250 mm; FOV phase = 100.0%; scan time = 7 min 24 s.

### 3.8. Molecular Modeling Method

The atomic structure of MDR2 (also known as multidrug resistance-associated protein; MRP2) was accessed on September 1, 2022, and downloaded from the AlphaFold protein structure database in the pdb file format (<https://alphafold.ebi.ac.uk/entry/Q92887>). The atomic structures of OATP1B1 and OATP1B3 were predicted using the SWISS-MODEL homology modeling server (<https://swissmodel.expasy.org/>). The docking software used in this research were AutoDock MGLTools 1.5.7 (<https://ccsb.scripps.edu/mgltools/>), AutoDock Vina 1.1.2 (<https://vina.scripps.edu/>), RDKit (<https://www.rdkit.org/>), and Open-source PyMOL (<https://github.com/schrodinger/pymol-open-source>). Four ligands—**Mn-NOTA-NP**, Mn-EDTA-BTA, Mn-EDTA-EOB, and Gd-DTPA-EOB—were prepared, minimized in three-dimensional structures, and saved in the pdbqt file format by adding polar hydrogen and fixing charges. AutoDock Vina was primarily used for docking ligands into target proteins. The application searches for space boxes in the coordinate system of a specific area and predicts the binding ability of binding models. AutoDock Vina employed a grid space of 1.000 Å for all runs. The population size was set to 150 and the number of genetic algorithms to 27,000 in AutoDock Vina. The binding modes of the four ligands were generated and analyzed using open-source PyMOL.

### 3.9. Cell Culture

RAW 264.7 (mouse monocyte/macrophage cells, Catalog No. ATCC®CRL-2278) was obtained from ATCC (Manassas, VA, USA) and cultured in accordance with the manufacturer's instructions. In addition, RAW 264.7 cells were cultured in RPMI-1640 medium obtained from Welgene (Daegu, Republic of Korea; Cat. LM011-01) containing 10% fetal bovine serum (FBS; Hyclone, Waltham, MA, USA; Catalog No. SH30919.03), and 1% penicillin-streptomycin solution (Gibco, Carlsbad, CA, USA; Catalog No. 11548876). Cells were cultured at 37 °C in a humidified incubator with a 5% CO<sub>2</sub> atmosphere.

### 3.10. Cell Viability Assay

The cytotoxicity of **Mn-NOTA-NP** and Gd-DTPA in mouse macrophage cells (RAW 264.7) was investigated. RAW 264.7 cells were plated in 96-well plates containing 100  $\mu\text{L}$  of complete media at  $1 \times 10^4$  cells/well. After 24 h, the medium was replaced with fresh medium containing varying concentrations of CAs (0, 0.5, 1, 5, 10, 25, 50, 100, and 200  $\mu\text{M}$ ), and the cells were incubated for another 22 h. The cells were then incubated for 2 h with CCK-8 solution (CCK-8, Dongin LS, Korea; Catalog No. CCK-3000). A microplate reader (SpectraMax i3, Molecular Devices, San Jose, CA, USA) was used to measure the absorbance at 450 nm.

### 3.11. Biodistribution

In total, 4 normal male Balb/c mice (7 weeks old, 20–25 g) were injected with 0.05 mmol/kg of **Mn-NOTA-NP** via the tail vein at various time points. The mice were anesthetized and sacrificed 15 min, 30 min, 1 h, and 24 h after injection. Mn levels were measured in the brain, heart, gallbladder, liver, kidneys, spleen, and intestine. Tissues were digested with 70%  $\text{HNO}_3$  and 30%  $\text{H}_2\text{O}_2$  at 180  $^\circ\text{C}$  for 2 h. The Mn content was measured in the resulting clear diluted solution (3% nitric acid) using inductively coupled plasma optical emission spectroscopy (ICP-OES) (Optima 7300DV, Perkin Elmer, Waltham, MA, USA). The detection limit of this method was set to 0.010 ppm.

### 3.12. In Vivo MRI of Normal Mice

All animal experiments were approved and performed in accordance with the guidelines of the Kyungpook National University Animal Care Committee. The MRI study used 6-week-old male Balb/c mice weighing 20–25 g. Mice were anesthetized with 1.5% isoflurane in oxygen. Measurements were recorded before and after the injection of paramagnetic complexes via the tail vein. After each measurement, the mouse was woken from anesthesia and placed in a cage with unlimited food and water. During measurements, the animals were maintained at room temperature. A 3 T MRI scanner (Architect, GE Healthcare, USA) equipped with a homemade small-animal radio frequency (RF) coil was used to capture the MR images. The imaging parameters for spin-echo were as follows: for coronal images, TR/TE/flip angle = 450 ms/8.8 FKimms/ $111^\circ$ , echo train length (ETL) = 3, matrix size =  $256 \times 192$ , FOV =  $80 \times 64$  mm, thickness = 1.2 mm, number of acquisitions (NEX) = 4; for axial images, TR/TE/flip angle = 450 ms/7.2 ms/ $111^\circ$ , ETL = 3, matrix size =  $192 \times 128$ , FOV =  $80 \times 64$  mm, thickness = 1.5 mm, NEX = 2.

### 3.13. Liver Tumor Model and In Vivo MRI

All animal experiments using the liver tumor model were performed with the approval of the Korea Institute of Radiological and Medical Sciences. To prepare an orthotopic xenograft model, HepG2 cells were harvested and resuspended in serum-free medium containing 50% Matrigel, and 6-week-old nude mice (Balb/c, male) from DooYeol Biotech (Seoul, Republic of Korea) were anesthetized with 3% isoflurane. HepG2 cells and Matrigel were inoculated into the left hepatic lobe of the mice. In vivo imaging was performed on the mice two months after inoculation. **Mn-NOTA-NP** was prepared as 50 mM stock solutions and used at a dose of 0.05 mmol [Mn/kg]. MR images were obtained at 3.0 T (Magnetom Tim Trio, Siemens, Germany) using a homemade 6-channel rat body coil. The imaging parameters were as follows:  $T_1$ -weighted 2D turbo spin echo (TSE) for coronal images, TR/TE/flip angle = 450 ms/10 ms/ $120^\circ$ , ETL = 3, matrix size =  $134 \times 192$ , FOV = 60 mm, slice thickness = 1 mm, number of averages = 6; for axial images, TR/TE/flip angle = 450 ms/9.3 ms/ $120^\circ$ , ETL = 3, matrix size =  $134 \times 192$ , FOV = 60 mm, slice thickness = 1.3 mm, number of averages = 4;  $T_2$ -weighted TSE, TR/TE/flip angle = 1620 ms/37 ms/ $120^\circ$ , matrix size =  $256 \times 256$ , FOV = 60 mm, slice thickness = 1 mm, number of averages = 4.

### 3.14. Image Analysis

On post-contrast MR images, anatomical positions with enhanced contrast were identified in the heart, liver, gallbladder, kidneys, and bladder. Additionally, signal intensities in specific regions of interest were measured quantitatively using Image J software (version 1.53e, National Institutes of Health, Bethesda, MD, USA). At each time point, the signal-to-noise ratio [ $SNR = P_{\text{signal}}/P_{\text{noise}}$ ] and contrast-to-noise ratio [ $CNR = SNR_{\text{post}} - SNR_{\text{pre}}$ ] were calculated for the relevant tissues of each mouse.

### 3.15. Statistical Analysis

One-way analysis of variance (ANOVA) with the nonparametric Mann–Whitney U test was used to analyze the data. GraphPad PRISM (version 5.03, GraphPad PRISM software Inc., San Diego, CA, USA) and SPSS (version 25, SPSS Inc., Chicago, IL, USA) were used for the analyses. Additionally, a MATLAB curve-fitting tool was used to fit the curves. Data are presented as mean  $\pm$  standard deviation (SD) or standard error of the mean (SEM) unless otherwise specified.

## 4. Conclusions

We developed a new macrocyclic  $Mn^{2+}$  complex comprising a  $\pi$ -conjugated naphthalene group and a NOTA-chelating ligand and evaluated its diagnostic potential as hepatobiliary MRI CAs. The in vivo biodistribution study and in vivo MRI investigation in mice suggested that **Mn-NOTA-NP** can promote excellent liver enhancement via a combination of hepatobiliary and renal clearance pathways, similar to that of Gd-DTPA-EOB. Moreover, in an HepG2 liver tumor model, **Mn-NOTA-NP** demonstrated enhanced tumor detection with paradoxically high tumor signal intensity. Additionally, ligand-binding simulations revealed that **Mn-NOTA-NP** binds to the transporters in a different manner than the other hepatobiliary agents investigated in this study. Hence, we believe that **Mn-NOTA-NP** can be an excellent alternative to  $Gd^{3+}$ -based hepatobiliary agents because it exhibits optimal properties as a liver-specific MRI agent.

**Supplementary Materials:** The following supporting information can be downloaded at: <https://www.mdpi.com/article/10.3390/ph16040602/s1>, Figure S1:  $^1H$  NMR spectrum of compound 2; Figure S2:  $^{13}C$  NMR spectrum of compound 2; Figure S3: High-resolution mass spectrum of compound 2; Figure S4:  $^1H$  NMR spectrum of compound 3; Figure S5: High-resolution mass spectrum of compound 3; Figure S6:  $^1H$  NMR spectrum of compound **NOTA-NP**; Figure S7:  $^{13}C$  NMR spectrum of compound **NOTA-NP**; Figure S8: High-resolution mass spectrum of compound **NOTA-NP**; Figure S9: HR-ESI-MS spectrum of compound **Mn-NOTA-NP**; Figure S10: HPLC spectrum of compound **Mn-NOTA-NP**; Figure S11: HSA binding of **Mn-NOTA-NP**; Figure S12: pH stability of **Mn-NOTA-NP**; Figure S13: Schematic representations of variable interactions between Mn-EDTA-BTA and (a) OATP1B1, (b) OATP1B3, and (c) MRP2 transporters; Figure S14: Schematic representations of variable interactions between (a) Mn-EDTA-EOB and (b) Gd-DTPA-EOB with MRP2 transporter.

**Author Contributions:** Conceptualization, M.K.I. and Y.C.; methodology, M.K.I., A.-R.B., B.-W.Y., S.K. and D.W.H.; investigation, M.K.I., A.-R.B., B.-W.Y., S.K. and D.W.H.; formal analysis, G.-H.L.; data curation, S.-W.N.; writing—original draft preparation, M.K.I.; writing—review and editing, G.-H.L. and Y.C.; supervision, Y.C.; funding acquisition, G.-H.L. and Y.C. All authors have read and agreed to the published version of the manuscript.

**Funding:** This work was supported by the National Research Foundation of Korea (NRF) grant (RS-2023-00207902), funded by the Korean government (MSIT). This work was also supported by the Basic Science Research Program of the NRF, funded by the Korean government (MSIT) (No. 2021R1A4A1029433).

**Institutional Review Board Statement:** The animal study protocol was approved by the Institutional Review Board (or Ethics Committee) of Kyungpook National University (2022-0345) and the Korea Institute of Radiological and Medical Sciences (2021-0077, approved on October 2021).

**Informed Consent Statement:** Not applicable.

**Data Availability Statement:** Not applicable.

**Conflicts of Interest:** The authors declare no conflict of interest.

## References

1. Gupta, A.; Caravan, P.; Price, W.S.; Platas-Iglesias, C.; Gale, E.M. Applications for Transition-Metal Chemistry in Contrast-Enhanced Magnetic Resonance Imaging. *Inorg. Chem.* **2020**, *59*, 6648–6678. [[CrossRef](#)] [[PubMed](#)]
2. Wahsner, J.; Gale, E.M.; Rodriguez-Rodriguez, A.; Caravan, P. Chemistry of MRI Contrast Agents: Current Challenges and New Frontiers. *Chem. Rev.* **2019**, *119*, 957–1057. [[CrossRef](#)] [[PubMed](#)]
3. Kim, H.K.; Lee, G.H.; Chang, Y. Gadolinium as an MRI contrast agent. *Future Med. Chem.* **2018**, *10*, 639–661. [[CrossRef](#)] [[PubMed](#)]
4. Matos, A.P.; Velloni, F.; Ramalho, M.; AlObaidy, M.; Rajapaksha, A.; Semelka, R.C. Focal liver lesions: Practical magnetic resonance imaging approach. *World J. Hepatol.* **2015**, *7*, 1987. [[CrossRef](#)]
5. Petitclerc, L.; Sebastiani, G.; Gilbert, G.; Cloutier, G.; Tang, A. Liver fibrosis: Review of current imaging and MRI quantification techniques. *J. Magn. Reson. Imaging* **2017**, *45*, 1276–1295. [[CrossRef](#)] [[PubMed](#)]
6. Ichikawa, T. Contrast-Enhanced Magnetic Resonance Imaging of the Liver and Pancreas. In *Medical Imaging Contrast Agents: A Clinical Manual*; Springer: Berlin/Heidelberg, Germany, 2021; pp. 131–148.
7. Grobner, T. Gadolinium—A specific trigger for the development of nephrogenic fibrosing dermopathy and nephrogenic systemic fibrosis? *Nephrol. Dial. Transplant.* **2006**, *21*, 1104–1108. [[CrossRef](#)] [[PubMed](#)]
8. Jost, G.; Frenzel, T.; Boyken, J.; Schoeckel, L.; Pietsch, H. Gadolinium presence in the brain after administration of the liver-specific gadolinium-based contrast agent gadoxetate: A systematic comparison to multipurpose agents in rats. *Investig. Radiol.* **2019**, *54*, 468–474. [[CrossRef](#)]
9. Lux, J.; Sherry, A.D. Advances in gadolinium-based MRI contrast agent designs for monitoring biological processes in vivo. *Curr. Opin. Chem. Biol.* **2018**, *45*, 121–130. [[CrossRef](#)]
10. Anbu, S.; Hoffmann, S.H.L.; Carniato, F.; Kenning, L.; Price, T.W.; Prior, T.J.; Botta, M.; Martins, A.F.; Stasiuk, G.J. A Single-Pot Template Reaction Towards a Manganese-Based T1 Contrast Agent. *Angew. Chem.* **2021**, *60*, 10736–10744. [[CrossRef](#)]
11. Ndiaye, D.; Sy, M.; Pallier, A.; Meme, S.; de Silva, I.; Lacerda, S.; Nonat, A.M.; Charbonniere, L.J.; Toth, E. Unprecedented Kinetic Inertness for a Mn(2+) -Bispidine Chelate: A Novel Structural Entry for Mn(2+) -Based Imaging Agents. *Angew. Chem.* **2020**, *59*, 11958–11963. [[CrossRef](#)]
12. Sun, C.; Yang, Z.; Wu, P.; Luo, X.; Liu, K.; Wang, B.; Lin, H.; Gao, J. Multinuclear Mn (II) united-DOTA complexes with enhanced inertness and high MRI contrast ability. *Cell Rep. Phys. Sci.* **2022**, *3*, 100920. [[CrossRef](#)]
13. Davis, K.A.; Lazar, B. Manganese-Based Contrast Agents as a Replacement for Gadolinium. *Radiol. Technol.* **2021**, *93*, 36–45. [[PubMed](#)]
14. Merbach, A.E.H.L.; Tóth, E. *The Chemistry of Contrast Agent in Medical Magnetic Resonance Imaging*; John Wiley & Sons: Hoboken, NJ, USA, 2013; pp. 1–23.
15. Roth, J.; Ponzoni, S.; Aschner, M. Manganese homeostasis and transport. *Met. Ions Life Sci.* **2013**, *12*, 169–201. [[CrossRef](#)] [[PubMed](#)]
16. Kang, Y.S.; Gore, J.C. Studies of tissue NMR relaxation enhancement by manganese. Dose and time dependences. *Investig. Radiol.* **1984**, *19*, 399–407. [[CrossRef](#)]
17. Murakami, T.; Baron, R.L.; Peterson, M.S.; Oliver, J.H., 3rd; Davis, P.L.; Confer, S.R.; Federle, M.P. Hepatocellular carcinoma: MR imaging with mangafodipir trisodium (Mn-DPDP). *Radiology* **1996**, *200*, 69–77. [[CrossRef](#)]
18. Chen, K.; Li, P.; Zhu, C.; Xia, Z.; Xia, Q.; Zhong, L.; Xiao, B.; Cheng, T.; Wu, C.; Shen, C.; et al. Mn(II) Complex of Lipophilic Group-Modified Ethylenediaminetetraacetic Acid (EDTA) as a New Hepatobiliary MRI Contrast Agent. *J. Med. Chem.* **2021**, *64*, 9182–9192. [[CrossRef](#)] [[PubMed](#)]
19. Islam, M.K.; Kim, S.; Kim, H.K.; Kim, Y.H.; Lee, Y.M.; Choi, G.; Baek, A.R.; Sung, B.K.; Kim, M.; Cho, A.E.; et al. Synthesis and Evaluation of Manganese(II)-Based Ethylenediaminetetraacetic Acid-Ethoxybenzyl Conjugate as a Highly Stable Hepatobiliary Magnetic Resonance Imaging Contrast Agent. *Bioconjugate Chem.* **2018**, *29*, 3614–3625. [[CrossRef](#)] [[PubMed](#)]
20. Islam, M.K.; Kim, S.; Kim, H.K.; Park, S.; Lee, G.H.; Kang, H.J.; Jung, J.C.; Park, J.S.; Kim, T.J.; Chang, Y. Manganese Complex of Ethylenediaminetetraacetic Acid (EDTA)-Benzothiazole Aniline (BTA) Conjugate as a Potential Liver-Targeting MRI Contrast Agent. *J. Med. Chem.* **2017**, *60*, 2993–3001. [[CrossRef](#)]
21. Schmitt-Willich, H. Stability of linear and macrocyclic gadolinium based contrast agents. *Br. J. Radiol.* **2007**, *80*, 581–582. [[CrossRef](#)]
22. Wang, J.; Wang, H.; Ramsay, I.A.; Erstad, D.J.; Fuchs, B.C.; Tanabe, K.K.; Caravan, P.; Gale, E.M. Manganese-Based Contrast Agents for Magnetic Resonance Imaging of Liver Tumors: Structure-Activity Relationships and Lead Candidate Evaluation. *J. Med. Chem.* **2018**, *61*, 8811–8824. [[CrossRef](#)]
23. McMurphy, T.J.; Parmelee, D.J.; Sajiki, H.; Scott, D.M.; Ouellet, H.S.; Walovitch, R.C.; Tyeklar, Z.; Dumas, S.; Bernard, P.; Nadler, S.; et al. The effect of a phosphodiester linking group on albumin binding, blood half-life, and relaxivity of intravascular diethylenetriaminepentaacetato aquo gadolinium(III) MRI contrast agents. *J. Med. Chem.* **2002**, *45*, 3465–3474. [[CrossRef](#)] [[PubMed](#)]

24. Gao, J.; Woolley, F.R.; Zingaro, R.A. In vitro anticancer activities and optical imaging of novel intercalative non-cisplatin conjugates. *J. Med. Chem.* **2005**, *48*, 7192–7197. [[CrossRef](#)] [[PubMed](#)]
25. Uzal-Varela, R.; Valencia, L.; Lalli, D.; Maneiro, M.; Esteban-Gomez, D.; Platas-Iglesias, C.; Botta, M.; Rodriguez-Rodriguez, A. Understanding the Effect of the Electron Spin Relaxation on the Relaxivities of Mn(II) Complexes with Triazacyclononane Derivatives. *Inorg. Chem.* **2021**, *60*, 15055–15068. [[CrossRef](#)]
26. Geraldès, C.; Sherry, A.; Brown III, R.; Koenig, S. Magnetic field dependence of solvent proton relaxation rates induced by Gd<sup>3+</sup> and Mn<sup>2+</sup> complexes of various polyaza macrocyclic ligands: Implications for NMR imaging. *Magn. Reson. Med.* **1986**, *3*, 242–250. [[CrossRef](#)] [[PubMed](#)]
27. Cacheris, W.; Nickle, S.; Sherry, A. Thermodynamic study of lanthanide complexes of 1,4,7-triazacyclononane-N, N', N''-triacetic acid and 1,4,7,10-tetraazacyclododecane-N, N', N'', N'''-tetraacetic acid. *Inorg. Chem.* **1987**, *26*, 958–960. [[CrossRef](#)]
28. Drahos, B.; Lukes, I.; Toth, E. Manganese(II) Complexes as Potential Contrast Agents for MRI. *Eur. J. Inorg. Chem.* **2012**, *2012*, 1975–1986. [[CrossRef](#)]
29. Hyon Bin Na, I.C.S. Taeghwan Hyeon. Inorganic Nanoparticles for MRI Contrast Agents. *Adv. Mater.* **2009**, *21*, 2133–2148.
30. Zhou, Z.; Zhao, Z.; Zhang, H.; Wang, Z.; Chen, X.; Wang, R.; Chen, Z.; Gao, J. Interplay between longitudinal and transverse contrasts in Fe<sub>3</sub>O<sub>4</sub> nanoparticles with (111) exposed surfaces. *ACS Nano* **2014**, *8*, 7976–7985. [[CrossRef](#)]
31. Kim, H.K.; Kang, M.K.; Jung, K.H.; Kang, S.H.; Kim, Y.H.; Jung, J.C.; Lee, G.H.; Chang, Y.; Kim, T.J. Gadolinium complex of DO3A-benzothiazole aniline (BTA) conjugate as a theranostic agent. *J. Med. Chem.* **2013**, *56*, 8104–8111. [[CrossRef](#)]
32. Rohrer, M.; Bauer, H.; Mintorovitch, J.; Requardt, M.; Weinmann, H.J. Comparison of magnetic properties of MRI contrast media solutions at different magnetic field strengths. *Investig. Radiol.* **2005**, *40*, 715–724. [[CrossRef](#)]
33. Waring, M.J. Lipophilicity in drug discovery. *Expert Opin. Drug Discov.* **2010**, *5*, 235–248. [[CrossRef](#)]
34. Baranyai, Z.; Brucher, E.; Uggeri, F.; Maiocchi, A.; Toth, I.; Andras, M.; Gaspar, A.; Zekany, L.; Aime, S. The role of equilibrium and kinetic properties in the dissociation of Gd[DTPA-bis(methylamide)] (Omniscan) at near to physiological conditions. *Chemistry* **2015**, *21*, 4789–4799. [[CrossRef](#)]
35. Gale, E.M.; Atanasova, I.P.; Blasi, F.; Ay, I.; Caravan, P. A Manganese Alternative to Gadolinium for MRI Contrast. *J. Am. Chem. Soc.* **2015**, *137*, 15548–15557. [[CrossRef](#)]
36. Federle, M.P.; Chezmar, J.L.; Rubin, D.L.; Weinreb, J.C.; Freeny, P.C.; Semelka, R.C.; Brown, J.J.; Borrello, J.A.; Lee, J.K.; Mattrey, R. Safety and efficacy of mangafodipir trisodium (MnDPDP) injection for hepatic MRI in adults: Results of the US multicenter phase III clinical trials (safety). *J. Magn. Reson. Imaging* **2000**, *12*, 186–197. [[CrossRef](#)]
37. Aime, S.; Gianolio, E.; Terreno, E.; Giovenzana, G.; Pagliarin, R.; Sisti, M.; Palmisano, G.; Botta, M.; Lowe, M.; Parker, D. Ternary Gd (III) L-HSA adducts: Evidence for the replacement of inner-sphere water molecules by coordinating groups of the protein. Implications for the design of contrast agents for MRI. *J. Biol. Inorg. Chem.* **2000**, *5*, 488–497. [[CrossRef](#)] [[PubMed](#)]
38. Meng, X.-Y.; Zhang, H.-X.; Mezei, M.; Cui, M. Molecular docking: A powerful approach for structure-based drug discovery. *Curr. Comput. -Aided Drug Des.* **2011**, *7*, 146–157. [[CrossRef](#)]
39. Pascolo, L.; Petrovic, S.; Cupelli, F.; Bruschi, C.V.; Anelli, P.L.; Lorusso, V.; Visigalli, M.; Uggeri, F.; Tiribelli, C. ABC protein transport of MRI contrast agents in canalicular rat liver plasma vesicles and yeast vacuoles. *Biochem. Biophys. Res. Commun.* **2001**, *282*, 60–66. [[CrossRef](#)] [[PubMed](#)]
40. Harwood, M.; Neuhoff, S.; Carlson, G.; Warhurst, G.; Rostami-Hodjegan, A. Absolute abundance and function of intestinal drug transporters: A prerequisite for fully mechanistic in vitro-in vivo extrapolation of oral drug absorption. *Biopharm. Drug Dispos.* **2013**, *34*, 2–28. [[CrossRef](#)]
41. Leonhardt, M.; Keiser, M.; Oswald, S.; Kühn, J.; Jia, J.; Grube, M.; Kroemer, H.K.; Siegmund, W.; Weitschies, W. Hepatic uptake of the magnetic resonance imaging contrast agent Gd-EOB-DTPA: Role of human organic anion transporters. *Drug Metab. Dispos.* **2010**, *38*, 1024–1028. [[CrossRef](#)] [[PubMed](#)]
42. Buxhofer-Ausch, V.; Secky, L.; Wlcek, K.; Svoboda, M.; Kounnis, V.; Briasoulis, E.; Tzakos, A.G.; Jaeger, W.; Thallhammer, T. Tumor-specific expression of organic anion-transporting polypeptides: Transporters as novel targets for cancer therapy. *J. Drug Deliv.* **2013**, *2013*, 863539. [[CrossRef](#)]
43. Idee, J.M.; Fretellier, N.; Robic, C.; Corot, C. The role of gadolinium chelates in the mechanism of nephrogenic systemic fibrosis: A critical update. *Crit. Rev. Toxicol.* **2014**, *44*, 895–913. [[CrossRef](#)] [[PubMed](#)]
44. Baek, A.R.; Kim, H.K.; Park, S.; Lee, G.H.; Kang, H.J.; Jung, J.C.; Park, J.S.; Ryeom, H.K.; Kim, T.J.; Chang, Y. Gadolinium Complex of 1,4,7,10-Tetraazacyclododecane-1,4,7-trisacetic Acid (DO3A)-Ethoxybenzyl (EOB) Conjugate as a New Macrocyclic Hepatobiliary MRI Contrast Agent. *J. Med. Chem.* **2017**, *60*, 4861–4868. [[CrossRef](#)]
45. Baek, A.R.; Kim, H.-K.; Kim, S.; Yang, J.-u.; Kang, M.-K.; Lee, J.J.; Sung, B.; Lee, H.; Kim, M.; Cho, A.E. Effect of Structural Fine-Tuning on Chelate Stability and Liver Uptake of Anionic MRI Contrast Agents. *J. Med. Chem.* **2022**, *65*, 6313–6324. [[CrossRef](#)] [[PubMed](#)]
46. Ni, Y.; Marchal, G.; Yu, J.; Muhler, A.; Lukito, G.; Baert, A.L. Prolonged positive contrast enhancement with Gd-EOB-DTPA in experimental liver tumors: Potential value in tissue characterization. *J. Magn. Reson. Imaging* **1994**, *4*, 355–363. [[CrossRef](#)] [[PubMed](#)]

47. Tsuboyama, T.; Onishi, H.; Kim, T.; Akita, H.; Hori, M.; Tatsumi, M.; Nakamoto, A.; Nagano, H.; Matsuura, N.; Wakasa, K. Hepatocellular carcinoma: Hepatocyte-selective enhancement at gadoteric acid-enhanced MR imaging—Correlation with expression of sinusoidal and canalicular transporters and bile accumulation. *Radiology* **2010**, *255*, 824–833. [[CrossRef](#)] [[PubMed](#)]
48. Ni, Y.; Marchal, G. Enhanced magnetic resonance imaging for tissue characterization of liver abnormalities with hepatobiliary contrast agents: An overview of preclinical animal experiments. *Top. Magn. Reson. Imaging TMRI* **1998**, *9*, 183–195. [[CrossRef](#)] [[PubMed](#)]

**Disclaimer/Publisher’s Note:** The statements, opinions and data contained in all publications are solely those of the individual author(s) and contributor(s) and not of MDPI and/or the editor(s). MDPI and/or the editor(s) disclaim responsibility for any injury to people or property resulting from any ideas, methods, instructions or products referred to in the content.